communications physics

ARTICLE

https://doi.org/10.1038/s42005-022-01015-w OPEN

Non-Hermitian skin clusters from strong interactions

Ruizhe Shen [1] & Ching Hua Lee [1✉]

Strong, non-perturbative interactions often lead to new exciting physics, as epitomized by emergent anyons from the Fractional Quantum hall effect. Within the actively investigated domain of non-Hermitian physics, we provide a family of states known as non-Hermitian skin clusters. Taking distinct forms as Vertex, Topological, Interface, Extended and Localized skin clusters, they generically originate from asymmetric correlated hoppings on a lattice, in the strongly interacting limit with quenched single-body energetics. Distinct from non-Hermitian skin modes which accumulate at boundaries, our skin clusters are predominantly translation invariant particle clusters. As purely interacting phenomena, they fall outside the purview of generalized Brillouin zone analysis, although our effective lattice formulation provides alternative analytic and topological characterization. Non-Hermitian skin clusters originate from the fragmentation structure of the Hilbert space and may thus be of significant interest in modern many-body contexts such as the Eigenstate thermalization hypothesis (ETH) and quantum scars.

[1] Department of Physics, National University of Singapore, Singapore 117542, Singapore. ✉email: phylch@nus.edu.sg

When many-body interactions dominate single-particle energetics, unexpected physics often emerge[1–12]. A classic example is the appearance of anyonic quasiparticles in Fractional Quantum hall (FQH) systems, whose emergent statistics cannot be inferred from single-particle Chern topology alone[12–18]. Indeed, the effects of strong non-perturbative interactions are determined by the structure[19–24] of the many-body Hilbert space, not the first-quantized single-particle description. Lately, research have focused on non-Hermitian phenomena. Yet, the main avenues of non-Hermiticity—the non-Hermitian skin effect (NHSE), which in general leads to eigenstate accumulations along boundaries[25–45] and exceptional points from spectral singularities[46–59]—are essentially single-particle mechanisms based on first-quantized notions like non-Bloch eigenstates and single-particle band structure[29,60–66]. It is thus timely to ask if strong interactions can open the door to even more exotic phenomena. While several works have explored many-body effects and interactions in non-Hermitian settings[67–69,69–73], interactions have not been the dominant physical mechanism.

In this work, we report the non-Hermitian skin clusters [Table 1] in the limit where interactions are much stronger than single-particle energetics. They are special translation invariant particle configurations, distinct from known non-Hermitian skin modes, being shaped by the connectivity structure of the many-body Hilbert space[19–21,74], not the real-space lattice, and do not even require physical boundaries. They possess features like the loop gap rather than the existing line gap or point gap. Such interacting phenomena cannot be understood via the generalized Brillouin zone (GBZ), which has been highly successful in characterizing conventional skin modes[27–30,33,75].

Results and discussion

Emergent topology and non-locality in a minimal unbalanced two-body hopping model. To understand how non-perturbative non-Hermitian interactions can lead to skin clusters states, we introduce a minimal 1D bosonic model purely consisting of unbalanced two-body correlated hoppings. Single-particle energetics are assumed to have been quenched, analogous to the scenario of dispersionless Landau levels[76–81]. Our model contains the four simplest possible asymmetric two-body hoppings, such that one particle hops across one site and the other hops across two sites in the opposite direction: [Fig. 1a]:

$$H = \sum_i^L (t_1+\gamma)c_{i+2}^\dagger c_i c_{i-1}^\dagger c_i + (t_1-\gamma)c_i^\dagger c_{i+2} c_i^\dagger c_{i-1} + (t_2-\gamma)c_{i+1}^\dagger c_i c_{i-2}^\dagger c_i + (t_2+\gamma)c_i^\dagger c_{i+1} c_i^\dagger c_{i-2} \quad (1)$$

Table 1 Characterization of non-Hermitian skin clusters. The 7 types of boundary states of our two-boson hopping model *H* in Eq.(1), with the 5 types of unconventional states (3–7).

	Type of state	Location	OBC/PBC
1	Topological edge mode	Physical boundary	OBC
2	Skin edge mode	Physical boundary	OBC
3	Vertex skin cluster	Intersection	OBC
4	Topological skin cluster	Effective interface	OBC
5	Interface skin cluster	Effective interface	PBC
6	Extended skin cluster	Effective interface	PBC
7	Localized skin cluster	Non-local region	PBC

Vertex (3) and Topological (4) skin clusters require both effective and physical boundaries [Fig. 2a for open boundary conditions (OBCs)]. Interface (5), Extended (6), and Localized (7) skin clusters are purely due to the effective interface in *H* [Fig. 3a for periodic boundary conditions (PBCs)]. Only (1) and (2) have been reported in the literature. The states (3), (4) and (5) are specific to 3-boson clusters, while states (6) and (7) can exist in generic $N > 2$-boson clusters (see Supplementary Note 1 for more details).

where $\hat{c}_i(\hat{c}_i^\dagger)$ is the bosonic annihilation (creation) operator at the i-th site. The non-Hermiticity is controlled by γ; when $\gamma = 0$, each hopping process and its reverse occur with equal probability t_1 or t_2, depending on the direction of center-of-mass translation. Although this Hamiltonian may superficially resemble NHSE models with asymmetric single-particle hoppings, i.e., the Hatano-Nelson model[26,37], it does not even act on single-particle states, implying that any skin cluster eigenstate must originate exclusively from particle-particle interactions.

The many-body Hilbert space of our model can be systematically dissected by identifying its various subsectors and how they are coupled[82]. We start by observing that each two-boson sector harbors hidden $\mathbb{Z}$ topology associated with 1D chiral symmetry. To concretely see that, note that two bosons only interact if they are either on the same site or three sites apart [Fig. 1a]. Hence, by restricting to only such configurations [Fig. 1b], we can index the 2-boson subspace as an effective *single*-body 1D chain [Fig. 1c] in configuration space. To see that, we take a two-boson state, $\psi(x_1, x_2)$, which is identified with $\psi(x_2, x_1)$ due to bosonic asymmetry, located at sites x_1 and $x_2 \geq x_1$, and introduce a relabeling $\Psi(X(x_1, x_2))$ for the same state, as given by

$$X(x_1,x_2) = \begin{cases} 2i-3 & \text{if} \quad x_2 = x_1 = i, \\ 2i-2 & \text{if} \quad x_2 = i+2, x_1 = i-1 \end{cases} \quad (2)$$

that captures configurations (x_1, x_2) acted by H. All other configurations decouple trivially. As illustrated in Fig. 1c and elaborated in the "Methods" section, the 2-boson sector reduces to an effective 1D non-Hermitian Su-Schrieffer-Heeger (SSH) chain with asymmetric couplings proportional to $t_1 \pm \gamma$ and $t_2 \pm \gamma$, since odd sites physically represent double bosonic occupancy and even sites represent bosons separated by three physical lattice spacings. We emphasize that generic models with asymmetric multi-particle hoppings often also contain variants of generalized SSH models[27,83,84].

The merits of our abovementioned basis relabeling become evident when we consider three or more particles. Key features of the many-body Hilbert space structure already emerge in a 3-boson sector. We write a three-boson state as $\psi(x_1, x_2, x_3) = \Psi(X(x_1, x_2), x_3)$, with permuted particle coordinates understood to correspond to the same state. A 3-boson sector then becomes a collection of coupled non-Hermitian SSH chains indexed by x_3 [Fig. 1b]. Their effective couplings come in two types: (i) dashed asymmetric couplings representing physical 2-body couplings between x_3 and x_1 or x_2, weighted by boson degeneracy factors such as $\sqrt{2!}, \sqrt{2!^2}$ and $\sqrt{3!}$, and (ii) solid double arrows representing pairs of identified sites that correspond to the same physical site due to bosonic symmetry, i.e. $(X(x_1, x_2), x_3)$ and $(X(x_2, x_3), x_1)$ for $x_2 = x_1 + 3 = x_3 - 3$. Also, due to bosonic symmetry, some asymmetric couplings become effectively non-local in the resultant lattice. For instance, consider three bosons, two close together and acted by a local physical interaction, and the third far away from both. However, due to symmetry under particle exchange, we have an equivalent description where the faraway boson is swapped with one of the nearby bosons, such that the local interaction appears as a non-local effective interaction.

Skin cluster states and Hilbert space fragmentation. Since interactions are reduced to ordinary hoppings on the effective lattice that represents the physically interesting many-body sector, they can be understood in terms of single-particle concepts. We show in Fig. 1e, f the Hilbert space connectivity under open boundary conditions (OBCs) and periodic boundary conditions (PBCs), for 2-boson and 3-boson subspaces, respectively (see

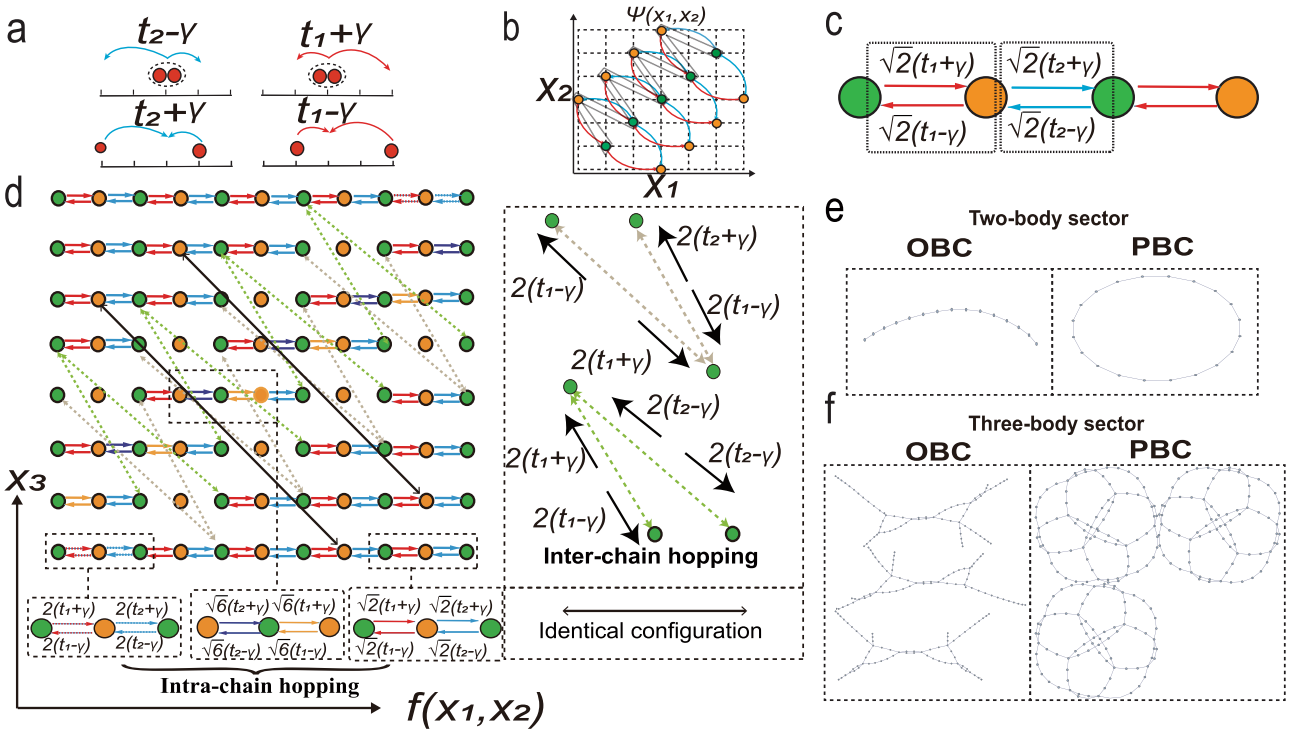

Fig. 1 Representations of models for the Hamiltonian in Eq.(1) in the real space and the effective graph. Sketch of effective models from correlated hoppings in Eq. (1). **a** The four asymmetric two-body hoppings in our interacting model [Eq. (1)], non-Hermitian whenever $\gamma \neq 0$. **b** Two-boson configurations (x_1, x_2), which are non-trivially coupled form a 1D subspace represented by a non-Hermitian effective Su-Schrieffer-Heeger (SSH) model **c** of $2L-5$ (see methods), where L is the number of sites in the physical OBC chain. **d** Effective 2D lattice for a 3-boson OBC subspace, which comprises an array of non-Hermitian SSH chains that are non-locally coupled by inter-chain hoppings (brown and green dashed double arrows), with certain physically identical configurations (black solid double arrows) (($X(x_1, x_2), x_3$) and permutations) identified. See Supplementary Note 1 for details of the effective 2D lattice. The labeled "intra-chain hoppling" is induced by bosonic statistics (see explanations in Supplementary Note 1). The "identical configuration" as the black double arrow is explained in the "Methods" section. **e**, **f** The Hilbert space connectivity graphs of H in the 2 and 3-boson sectors for $L = 15$, demonstrating non-trivial modifications to the graph structure from open boundary condition (OBC) to periodic boundary condition (PBC) beyond two bosons.

Supplementary Note 2 for that of 4 and 5-boson subspaces). While the 2-body subspaces simply form 1D chains, as previously explained, the 3-body spaces decouple into three sectors, each containing some states that are not easily reached, suggestive of Hilbert space fragmentation[19–22,85–87]. For more than two particles, the Hilbert space connectivity graphs become much more complicated when going from OBCs to PBCs, much beyond merely "closing up" chains into loops. This hence hints of more exotic phenomena besides the conventional NHSE. Indeed, in the PBC case, there exists a hierarchy of smaller loops that are coupled only at a few selected states. When superimposed onto an effective lattice structure, these inter-loop couplings correspond to the previously mentioned effective non-local hoppings.

For concrete analysis of our specific model, we decompose the effective lattice of Fig. 1c into regions that take different roles in forming the skin clusters [Fig. 2a for OBCs, 3c for PBCs]. We shall focus on clusters with $N = 3$ bosons, and then discuss how some of them generalizes to generic N number of bosons. There exists a "non-local" region around $x_3 \approx X(x_1, x_2)$, which is crossed by a large number of non-local effective hoppings across several effective sites (diagonal effective hoppings in Fig. 1c, which hop across the cyan "non-local" region in Fig. 2a or Fig. 3a). They arise from physical interactions between a two-boson sector and a third boson. The background "local" region experiences only nearest-neighbor SSH-type effective hoppings (white in Figs. 2a and 3a) from 2-boson processes only. Note that all effective hoppings originate from the one and only type of interaction term present in H; the demarcation into "local" and "non-local" regions reflect the qualitatively different roles of processes involving different numbers of bosons. Non-local hoppings across the "non-local" region destroy the periodicity in the effective lattice, precluding any GBZ description that relates the distinct OBC and PBC spectra (Figs. 2b and 3b), unlike in non-interacting models.

Importantly, effective interfaces emerge between the "local" and "non-local" regions, in addition to physical boundaries at the edges of the effective lattice, if any. This results in additional localization behavior beyond topological and skin edge localizations. We identified seven distinct types of boundary states [Table 1]. As effective interfaces are induced by particle statistics, not physical boundaries, our states (Types (3) to (7)) are named "skin cluster states". Vertex skin clusters (3) are unique highly localized states at point intersections (vertices) of effective and physical boundaries [Fig. 2a], and are elaborated in Supplementary Note 1. Topological (4), Interface (5), Extended (6), and Localized (7) skin clusters represent distinct ways by which the effective interfaces exert topological and skin localization and will be elaborated below.

The five types of states from (3) to (7) in Table 1 are distinguished by the location at which they are localized in the effective space. Under OBCs, there exist "topological skin clusters" (see the blue mode in Fig. 2), which are mathematically equivalent to usual topological boundary modes at the physical boundaries. At the crossing point of the physical and effective boundary, the localization is further squeezed into highly localized "vertex skin clusters" represented as the pink mode in

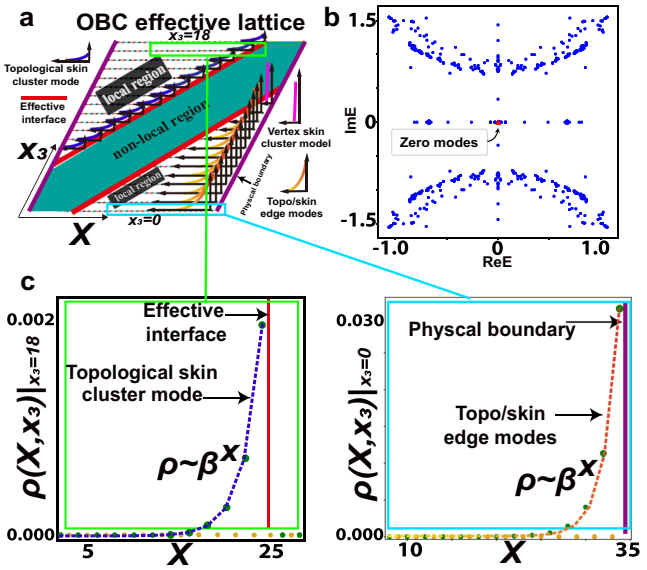

Fig. 2 Localizations in the effective lattic for the Hamiltonian in Eq.(1) under OBCs. Localizations in the effective lattice for the 3-boson sector under open boundary conditions (OBCs). **a** Schematic of the effective Hilbert space lattice for the 3-boson sector under OBCs. Regions with local (white) and non-local (cyan) effective hoppings are demarcated by the interaction-induced effective interfaces (red lines). Topological skin cluster modes accumulate against effective interfaces, while vertex skin clusters are localized at intersections between effective interfaces and physical edges (purple), which also host ordinary skin/topo edge modes. **b** The three-boson OBC spectrum with parameters $t_1 = 1.0, t_2 = 0.2, \gamma = 0.8$, on a $(2L-5) \times L$ effective lattice ($L = 20$). Zero modes correspond to either topological edge modes or skin clusters. **c** Spatial density profiles $\rho(X, x_3) = |\Psi(X, x_3)|^2$ of both types of topological modes, which clearly accumulate at either the effective interface or physical boundary with identical decay profiles $\rho(X, x_3) \sim \beta^X$, $\beta = (t_1 + \gamma)/(\gamma - t_2)$ (see methods). Green and yellow dots in **c** correspond to the horizontal even and odd sites in **a**. More details of the exponential localizations can be found in in Supplementary Note 1.

Fig. 2. When we consider PBCs, where the physical boundary is no longer present, we obtain more types of states without conventional OBC analogs. Instead of "topological skin clusters", we now have "interface skin clusters", "extended skin clusters" and "localized skin clusters", which are represented by gray, blue, and red modes in Fig. 3. As suggested by their name, "interface skin clusters" are highly localized at the effective boundaries, while the other two types, "localized skin clusters" and "extended skin clusters", appear in the coupled and noncoupled chains in the effective lattice. Among these five states, only the "localized skin clusters" and "extended skin clusters" have direct generalized in the higher dimensional Hilbert space of $N > 3$-boson clusters ($N > 3$-boson sector). We will further elaborate on these states in Fig. 5 below and surrounding paragraphs, as well as in Supplementary Note 1.

Although skin clusters also arise from asymmetric couplings, they differ from conventional NHSE skin states in a few important ways: (i) they only exist when two or more particles interact; (ii) they exist due to the inhomogeneity of effective couplings from particle statistics, *not* physical boundaries as in the NHSE[74]: in fact (5–7) exist under PBCs, not OBCs; (iii) while the NHSE usually gives rise to non-local responses[30,31,88], here the skin clusters themselves are already the consequence of non-local effective couplings; (iv) due to the "non-local" region, the various types of skin clusters do not possess GBZ descriptions, unlike ordinary skin states.

Topological skin clusters. Topological skin clusters eigenstates (4) are topological zero modes at the effective interface between the "local" and "non-local" regions. Physically, they are manifestations of how the inherent SSH-type topology in a 2-boson sector interplays with the presence of a third boson. Although effective interfaces exist identically across both OBC [Fig. 2] and PBC [Fig. 3] settings, Topological skin clusters only exist under OBCs. PBC skin clusters (5-7) differ significantly from them in both energetics [Figs. 2b vs. 3b] and spatial profile [Figs. 2c vs. 3c]. This enigma arises because of the non-local effect of local unbalanced hoppings: Under PBCs, the absence of physical boundaries (edges) leads to significant interference between the NHSE-like accumulation from either side of the non-local region, destroying "unadulterated" topological states. That topological skin clusters (4) mathematically result from the same topological mechanism as ordinary topological edge states (1) can be seen from their vanishing energies [Fig. 2b], and identical localization lengths [Fig. 2c] of $(\log\beta)^{-1}$, with $\beta = (t_1 + \gamma)/(\gamma - t_2)$ as is well-known for the non-Hermitian SSH model[27]. See "Methods" for edge states in the non-Hermitian SSH model.

Translation invariant skin clusters. Without physical boundaries (PBCs), the three types of skin clusters (5–7) that exist are of special non-topological origins. They are Interface (5), Extended (6) and Localized (7) skin cluster, so-called because they, respectively, exist at the interface between the "local" and "non-local" regions (5), are extended across the wide "local" region (6) or are localized within the relatively narrow "non-local" regions (7), as seen from $|\Psi(X(x_1, x_2), x_3)|^2$ density plots of Fig. 3c. Although Interface clusters (2) appear the most localized of the three on the effective lattice, in physical coordinates, their density plot $|\psi(x_1, x_2, x_3)|^2$ (Fig. 3c) reveal strong correlations between particles a few sites apart. By contrast, Localized skin clusters (7) consist of 3 bosons that are indeed almost physically overlapping, "caged" by the non-local effective hoppings. The extended skin clusters (6) are the most delocalized but are still considered clusters states because they are exponentially localized along the effective interface.

The eigenenergies of different types of skin cluster eigenstates generically form very distinct loci in the complex energy plane. As shown in Fig. 3b, extended and localized cluster states (6,7) form two concentric spectral loops, while the interface states (5) form isolated points in the loop interiors. Under parameter tuning, these characteristic spectral loci remain largely robust, even though they may distort and cross each other.

Structure of skin cluster states and the loop gap.– The concentric rings of eigenenergies in the 3-body PBC spectrum [Fig. 3b] are robust across a large range of parameters, and can even persist even beyond three bosons, as elaborated in Supplementary Note 1. We name this unmistakable separation of concentric PBC spectral loops as a *loop gap*, in the spirit of point gaps for loops, which encircle interior points[37]. To understand why the loop gap occurs, we note that the outer/inner spectral ring corresponds to localized/extended cluster states. In the fully localized limit where all bosons move rigidly like a single composite particle, the PBC spectrum traces out a large loop given by $E = \sum_j t_j e^{ipj}$, where $p \in [0, 2\pi)$ and t_j are the effective j-site hoppings acting on the composite particle. Compared to localized clusters, extended clusters must trace out smaller loops because at least one boson does not move in unison with the others [Fig. 3c], leading to "destructive interference". Note that localized and extended clusters move freely as a whole, unlike interface clusters and topological edge modes, which are constrained to specific physical locations. This causes the latter two to be spectrally enclosed within the localized

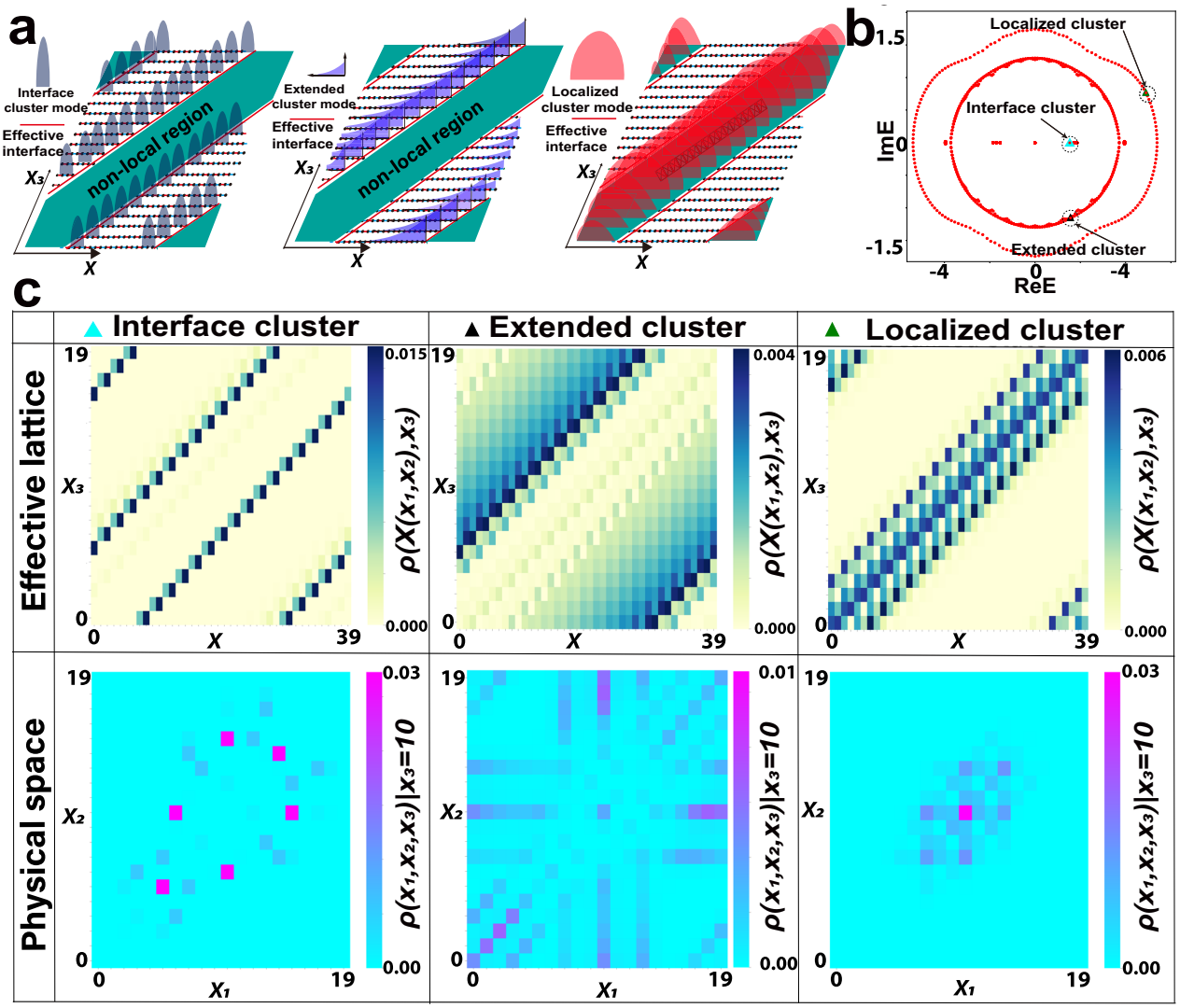

Fig. 3 Localizations in the effective lattic for the Hamiltonian in Eq.(1) under PBCs. Characterization of different clusters in the $N = 3$-boson sector under periodic boundary conditions (PBCs). **a** Schematics of the effective Hilbert space lattice for the 3-boson sector under PBCs, with each panel illustrating its respective type of PBC cluster mode. The effective interfaces in the red lines generate a "non-local region" in the lattice. Interface cluster modes (gray) and extended cluster modes (blue) appear at the boundary of the non-local region, whereas localized cluster modes exist in the bulk. **b** The three-boson PBC spectrum with parameters $t_1 = 1.4, t_2 = 1.2, \gamma = 0.5, L = 20$. Generally, localized cluster states form an outer loop with the largest $|E|$, separated from the inner loop of Extended skin clusters via a loop gap. Exact solutions for interface clusters form isolated spectra are given in Supplementary Note 1. **c** Numerically computed spatial density distribution of the three types of clusters. $\rho(X, x_3) = |\Psi(X(x_1, x_2), x_3)|^2$ represents the density in the effective lattice, and $\rho = |\psi(x_1, x_2, x_3)|^2_{x_3=10}$ is for the density in the physical lattice. The color bars in **c** indicate the amplitude of each type of density. Interface clusters, while seemingly constrained at the effective interface, actually consist of bosons several sites from each other. Extended clusters favor physical configurations with two overlapping bosons and another far away. Localized clusters contain bosons that are physically localized within sites from each other.

and extended clusters [Fig. 4a] since, being confined, they cannot be significantly amplified by the asymmetric hoppings and must thus possess energies close to $E = 0$.

The above arguments can be corroborated by the following 2 and 3-site density correlators, which reveal more insight into the real-space structure of the cluster states:

$$\begin{aligned}(a)\, C_m(x_i, x_j) &= \left|\langle\psi_m|n_i n_j|\psi_m\rangle\right|, (i \neq j)\\ (b)\, C_m(x_i, x_j, x_k) &= \left|\langle\psi_m|n_i n_j n_k|\psi_m\rangle\right|,\end{aligned} \tag{3}$$

where ψ_m is the selected eigenstate and the density operator $n_i = c_i^\dagger c_i$ measures the occupancy at site i. These correlators are plotted in Fig. 4b for representative eigenstates ψ_m as specified in Fig. 4a; to put their magnitudes in perspective, note that they scale, respectively, as L^{-2} and L^{-3} for a perfectly uniform state, but remain at unity for a perfectly clustered state. Comparing the 2-site-correlator $C_m(x_i, x_j)$ in Fig. 4b with the single-site density plots in Fig. 3c, both for the effective lattice, we observe similar trends despite the different model parameters and chosen states. However, $C_m(x_i, x_j)$ always reveals conspicuously strong spectral weights at the interfaces, suggesting that the bosons prefer to be separated by 3–5 sites regardless of the cluster type. The three site-correlator $C_m(x_i, x_j, x_k)$ further reveals that extended states tend to consist of 2 bosons on the same site, together with another arbitrarily far boson.

Effective interface and clustering in many-body sectors. Many results from the three-boson sector, which we elaborated above, continue to hold in sectors, i.e., clusters with arbitrarily number of bosons. In essence, effective boundaries in the N-body Hilbert space

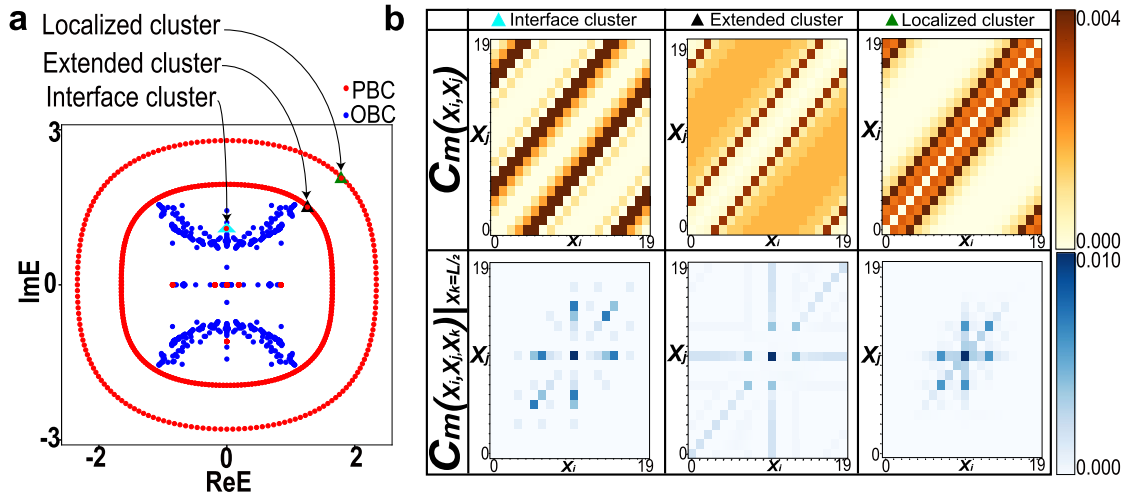

Fig. 4 Correlation behavior in Eq.(3) under OBCs and PBCs. Correlation behaviors for different clusters in the 3-boson sector under periodic boundary conditions (PBCs). **a** The 3-boson PBC spectrum (red) is characterized by a loop gap between concentric loops, which also enclose isolated PBC interface cluster energies and most of the OBC spectrum (blue). The selected localized, extended, and interface cluster are labeled in green, black, and blue triangular dots, respectively. **b** Density correlators for representative PBC eigenstates ψ_m of the three cluster types from **a**. 2-site correlators $C_m(x_i, x_j)$ in Eq. (3) (*a*) for $i \neq j$ reveal that interface configurations $|x_i - x_j| = 3$ are favored in all cluster types. 3-site $C_m(x_i, x_j, x_k)|_{x_k = L/2}$ in Eq. (3) (*b*) is evaluated at $x_k = L/2$. Without loss of generality, due to translation symmetry, reveal that extended clusters are most likely to have a doubly occupied site, but that localized clusters possess the shortest correlation range. Parameters are $t_1 = 1.0$, $t_2 = 0.2$, $\gamma = 0.8$, with $L = 20$. The color bars in **b** represent the amplitude of each correlator, respectively.

continue to play a crucial role, and are generalized to be regions of high connectivity that separate regions of different levels of connectivities. In this context, what is required is that there exists a contrast between the connectivities of the nodes in the many-body Hilbert space, rather than particular values of the connectivities. This is because the non-Hermitian skin cluster effect acts whenever there exists inhomogeneities in the Hilbert space graph, reminiscent of the usual non-Hermitian skin effect, which are non-perturbatively sensitive to any form of spatial inhomogeneity.

Shown in Fig. 5 are the Hilbert space graphs of $N = 3, 4$ and 5 bosons, as well as illustrative localized clusters and delocalized states. The graph in Fig. 5a is equivalent to the two-dimensional lattice in Fig. 3a. For the three-boson sector, we already know that the effective interface separates the graph into different connectivity regions (see Fig. 3). Similarly, for the four and five-boson sectors in Fig. 5e, f, i and j, analogous effective interfaces exist at regions of highest connectivities, such that they also separate regions of different connectivities (see Fig. 5d, h, l, dashed blue boxes). Generally, a node with more neighbors indicates that the corresponding state is a more strongly correlated state. Thus, the effective interface represents kinetic blockage constraints due to interactions (Fig. 5d). Such a notion of an effective boundary can be directly generalized to arbitrary number of particles. From Fig. 5c, g, and k, we also see that localized skin cluster states always exist on the outer spectral loop regardless of the number of particles, while other illustrative delocalized states exist within the loop gap. Around an effective interface, the states take the form of a cluster of particles that accumulate against each other, hence the name “skin cluster states”.

Conclusion

Our simple model with asymmetric two-body hoppings (Eq. (1)) is a paradigmatic representation of non-reciprocal non-Hermitian physics in the strongly interacting limit where single-body energetics are quenched. While asymmetric couplings have been associated with the well-known single-particle NHSE, our purely interacting model exhibits various clustering behavior [Table 1 (3–7)]. As a departure from conventional NHSE, these cluster states are mostly translation invariant, even if they require OBCs, as in topological skin clusters (4).

Stemming from effective interfaces in a fragmented Hilbert space, our states should exist in generic non-Hermitian interacting lattices with (i) asymmetric couplings and (ii) quenched single-particle energetics. Unlike in Hermitian models where the effective interfaces are physically significant only if they scale with the system size, our non-Hermitian effective interfaces can dramatically modify the system dynamics even if they are of vanishing fractal dimension in the Hilbert space, thanks to the profoundly non-perturbative and non-local nature of non-Hermitian skin clustering. As such, the Hilbert space fragmentation from non-Hermitian skin clustering, which violates the eigenstate thermalization hypothesis (ETH)[20,85,86,89], will likely inspire further study into the non-equilibrium dynamics in non-Hermitian systems, e.g., quantum many-body scars[85,90–94], and many-body localization[95–97]. Appropriately generalized, our model may be physically realized with density-assisted tunneling in driven optical lattices[91,98], quantum digital computer circuits with suitably arranged imaginary time evolution[99,100], or, topolectrical circuits[31,44,101–107] at the effective lattice level.

Methods

Two-boson sector as a non-Hermitian SSH chain. In order to deal with our non-Hermitian interacting model in Eq. (1), we apply its Hilbert space graph, which serves as an effective non-interacting model. In this section, we use a minimal two-body model for Eq. (1) to explain how the NHSE works in the Hilbert space graph. According to the analysis in the main text, the Hilbert space graph of the two-body model is the effective SSH chain. Here we furnish more details of this effective SSH chain, which indirectly controls the physics of the two bosons in physical space.

We consider the zero mode in the effective SSH chain, expressed as $\psi = (\psi_{1A}, \psi_{1B}, \ldots \ldots \psi_{n-1A}, \psi_{n-1B}, \psi_{nA})^T$ (A,B are the labels of the sublattices in Fig. 6). The sublattice wavefunction takes the exponential form $(\psi_{nA}, \psi_{nB})_T = \beta^n(\psi_{1A}, \psi_{1B})^T$ according to the generalized Brillouin zone ansatz[27,28]. In the bulk, the eigen-equation satisfies

$$\begin{aligned} \sqrt{2}(t_1 - \gamma)\psi_{iB} + \sqrt{2}(t_2 + \gamma)\psi_{i-1B} &= E\psi_{iA} \\ \sqrt{2}(t_1 + \gamma)\psi_{iA} + \sqrt{2}(t_2 - \gamma)\psi_{i+1A} &= E\psi_{iB} \end{aligned} \tag{4}$$

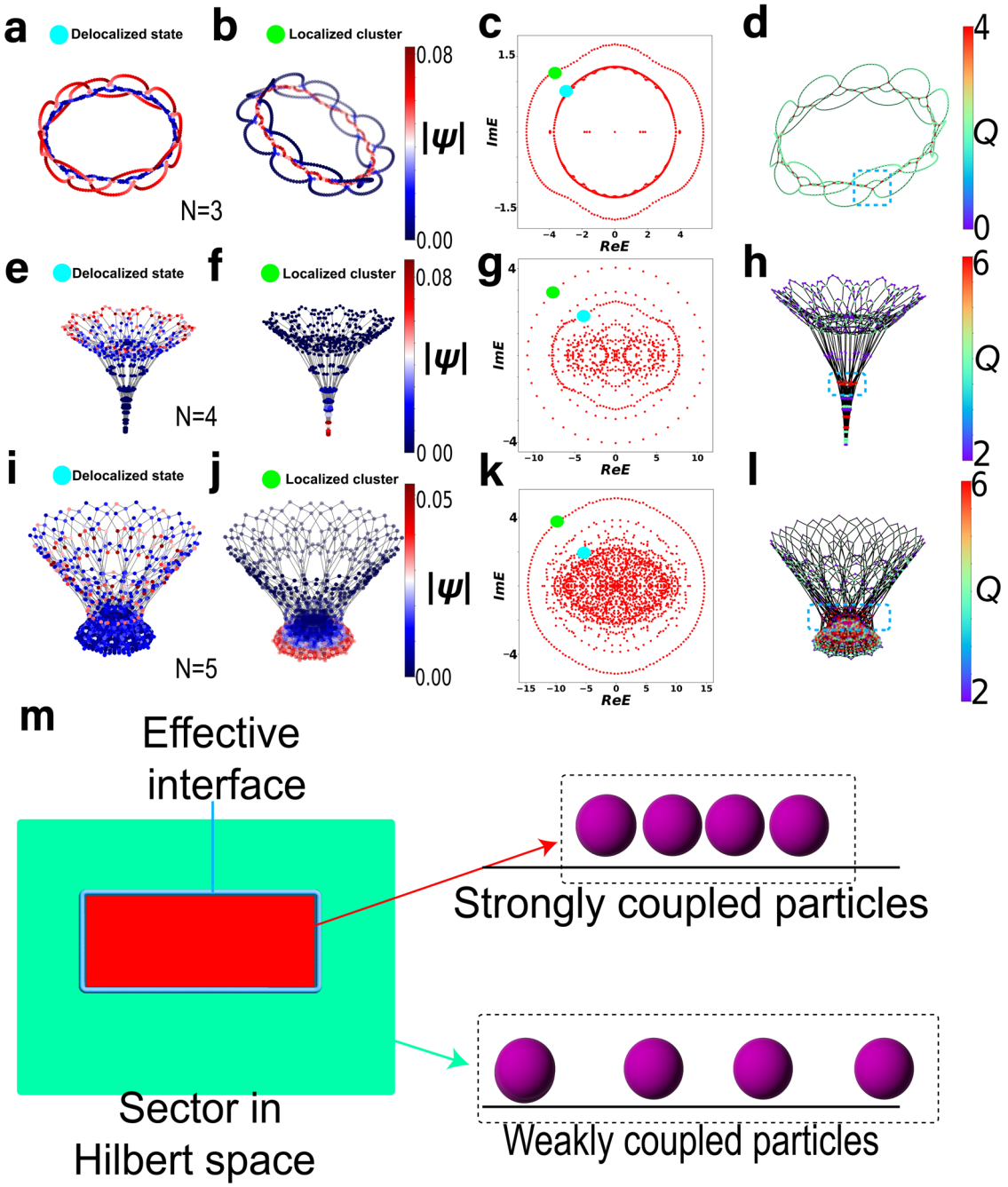

Fig. 5 Generalization of the effective interaface in the Hilbert space for the discussion in subsection "Effective interface and clustering in many-body sectors." from the section "result and discussion". Many-body Hilbert space graphs and the densities of selected cluster and delocalized non-cluster states in $N = 3, 4, 5$-boson sectors under periodic boundary conditions (PBCs). Plot **a** represents the delocalized state (state indicated by the light blue dot in **c**), and plot **b** depicts the localized cluster state (state indicated by the green dot in **c**). Plot **a** and **b** share the same color bar, which represents the amplitude of the wavefunction $|\psi|$ at each node. **c** is for the spectra under PBCs with the selected states for **a** and **b**. In plot **d**, the effective boundary highlighted in blue dashed box is the red region of higher connectivity (no. of graph neighbors Q identified in the color bar) that separates regions of relatively low connectivity. The representations for **e**–**h** and **i**–**l** follow the manner of the plots **a**–**d**. According to **a**–**l**, we find that localized cluster states always lie on the outer spectral loop regardless of the number of bosons N. Also, they always lie next to effective boundaries, which are regions of highest connectivity on the Hilbert space graph that also separates regions of relatively high and low connectivity. **m** Schematic notion of an "effective interface" in a Hilbert space graph: by separating regions of different levels of connectivity, it is physically interpreted as a demarcation between strongly and weakly coupled particles. The size and filling are **a**–**d** $L = 20$, $N = 3$; **e**–**h** $L = 10$, $N = 4$; **i**–**l** $L = 10$, $N = 5$. Parameters are $t_1 = 1.4$, $t_2 = 1.2$, $\gamma = 0.5$.

At the boundary, the OBC boundary condition gives

$$\begin{aligned}\sqrt{2}(t_1 - \gamma)\psi_{1B} &= E\psi_{1A}\\ \sqrt{2}(t_2 + \gamma)\psi_{n-1B} &= E\psi_{nA}.\end{aligned} \tag{5}$$

From them, we can obtain the solution to the zero mode of SSH chain as $\psi_{1B} = 0, \beta = (t_1 + \gamma)/(\gamma - t_2)$. Figure 6b presents a zero mode in the effective SSH chain while Fig. 6c presents its corresponding squared amplitude in physical space, as a two-boson system. Similarly, the three-boson sector can be mapped to a two-dimensional non-Hermitian model as shown in Fig. 1d. See more details of the effective two-dimensional non-Hermitian model in Supplementary Note 1.

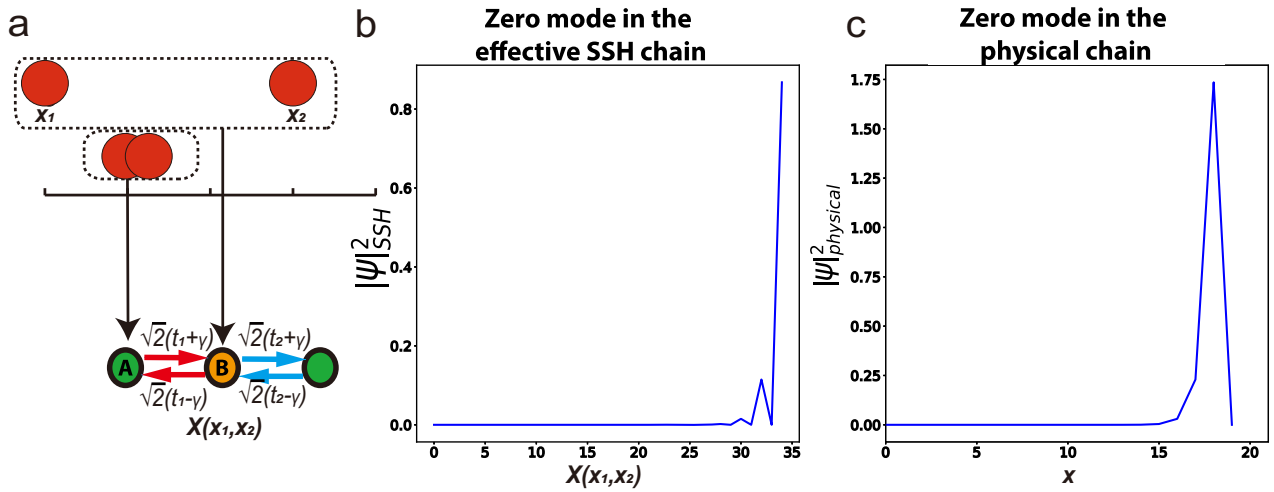

Fig. 6 Correspondence of skin modes from Eq. (4) in the real space and the effective chain. Correspondence of localizations in the real space and the effective chain for the two-boson sector under open boundary conditions (OBCs). **a** The Non-Hermitian effective SSH model corresponding to the physical two-boson model, and the corresponding two-boson state from the physical chain that maps to odd/even sites in the effective SSH chain. The squared amplitudes of the same zero mode in the effective chain **b** vs. the physical chain **c** with $t_1 = 1.2, t_2 = 0.2, \gamma = 1.0, L = 20$. The corresponding length of the effective SSH chain is $2L - 5$. $X(_1, x_2)$ in **b** is given in Eq. (2), and x in **c** represents the position in the physical space.

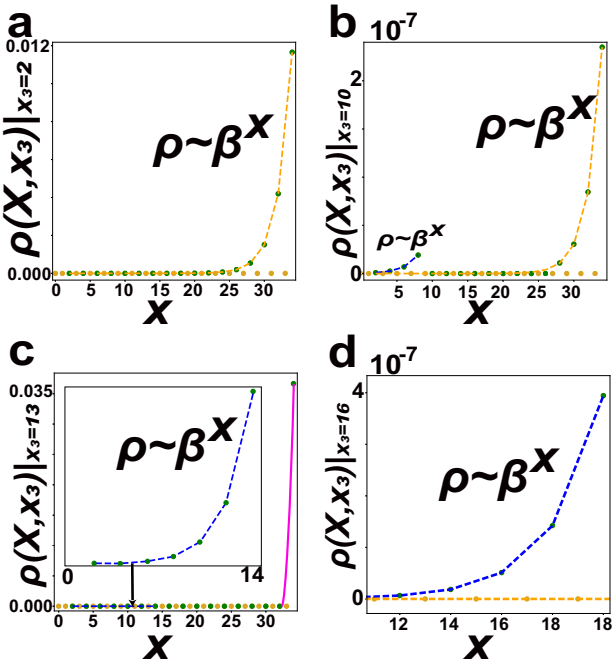

Fig. 7 Details of the skin localization in the effective for the subsection "Cluster states of topological origin" from the section "Method". Exponential localizations in the effective lattice for 3-boson cluster under open boundary conditions (OBCs). 2D cross-sectional density $\rho = |\Psi(X, x_3)|^2$ of the OBC effective lattice in Fig. 1d, with fixed $x_3 = 2$ (**a**), 10 (**b**), 13 (**c**), 16 (**d**) of selected states with $t_1 = 1.0, t_2 = 0.2, \gamma = 2.0, L = 20$. For the cases $x_3 = 2, 10$, there is skin localization at the physical boundary(the yellow curves). For the cases $x_3 = 10, 13, 16$, there is skin localization at the interface (the blue curves). Also present are the trivial mode and the vertex localization (the pink curve in **c**) at the intersection between the physical boundary and the interface in the effective lattice. All the blue and yellow curves exhibit the exponential localizations as $\rho \sim \beta^x$ with $\beta = (t_1 + \gamma)/(\gamma - t_2)$.

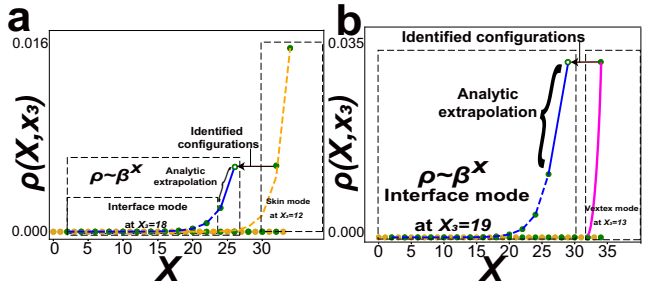

Fig. 8 Details of the discussion on the interface of the effective lattice for the subsection "Cluster states of topological origin" from the section "Method". Identified configurations from bosonic symmetry. **a** The yellow curve: the skin mode of $\rho(X, x_3) = |\Psi(X, x_3)|^2_{x_3=12}$; The blue curve: the interface mode of $\rho(X, x_3) = |\Psi(X, x_3)|^2_{x_3=18}$. The "Identified configurations" between sites allows us to move a section (the dashed rectangle) of the skin mode to the nearest site of the interface mode (the green hollow circle). We perform an analytic extrapolation (blue solid line) according to the non-Bloch scaling controlled by β (the solid blue line) to link the two ends. **b** The pink curve: the vertex mode of $\rho(X, x_3) = |\Psi(X, x_3)|^2_{x_3=13}$; The blue curve: the interface mode of $\rho(X, x_3) = |\Psi(X, x_3)|^2_{x_3=19}$. Exponential localizations as the blue and yellow curves follow the scaling $\rho(X, x_3) \sim \beta^X$ with $\beta = (t_1 + \gamma)/(\gamma - t_2)$. In our model, bosonic symmetry leads to equivalent "identified configurations" in the effective lattice in Fig. 1d, and hence skin cluster states on it that can be pieced together like a jigsaw-puzzle. The density as $\rho(X, x_3) = |\Psi(X, x_3)|^2$ represents the localization in the graph in Fig. 2a for the 3-boson cluster under open boundary conditions (OBCs). Parameters for **a** and **b** are $t_1 = 1.0, t_2 = 0.2, \gamma = 2.0$, and $L = 20$.

Cluster states of topological origin. In our effective lattice for 3 bosons under OBCs from the main text, there exists both physical boundaries and effective interfaces as shown in Fig. 2a. When $\gamma \neq 0$, localization occurs at both the two boundaries. Figure 7 presents the state amplitude distribution in the effective lattice of a selected OBC zero mode with $t_1 = 1.2, t_2 = 0.2, \gamma = 0.5, L = 20$.

To show that the localizations near the interface and the physical boundary have the same topological origin, we perform the curve fitting of these decays and compare the analytical result $\beta = (t_1 + \gamma)/(\gamma - t_2)$ (the solution of the effective non-Hermitian SSH model) with the curve fitted results from numerical diagonalization of the 3-body system. Indeed, for the zero modes of the three-body sector, the decays at the physical boundary (β') and effective interfaces (β'') all agree viz. $\beta'', \beta' \approx \beta$ ($\rho(x) \approx \beta^x$).

The interface within the effective lattice is demarcated by "identified configurations" arising from bosonic statistics (See the structure of the 2D lattice in Supplementary Note 1). So as to explain these interface localizations under OBC, we plot skin (vertex) modes and the interface mode connected by the "Identified configurations" together (Fig. 8). These results suggest that the interface mode is a branch of the skin (vertex) mode, such that we can use analytic extrapolation to attach the interface mode to a section of the skin (vertex) mode.

Data availability

The data that support the plots within this paper are available upon reasonable request.

Code availability

Computer codes used to generate the plots in this work are available upon reasonable request via email to C.H.L.

Received: 4 November 2021; Accepted: 12 September 2022;
Published online: 24 September 2022

References

1. Zhang, S. C., Hansson, T. H. & Kivelson, S. Effective-field-theory model for the fractional quantum hall effect. *Phys. Rev. Lett.* **62**, 82 (1989).
2. Jain, J. K. Composite-fermion approach for the fractional quantum hall effect. *Phys. Rev. Lett.* **63**, 199 (1989).
3. Jain, J. Theory of the fractional quantum hall effect. *Phys. Rev. B* **41**, 7653 (1990).
4. Wen, X.-G. Theory of the edge states in fractional quantum hall effects. *Int. J. Mod. Phys. B* **6**, 1711–1762 (1992).
5. Yu, L., Lundqvist, S. & Morandi, G. (eds) *Low-dimensional Quantum Field Theories For Condensed Matter Physicists-Lecture Notes Of Ictp Summer Course*. Vol. 6. (World Scientific, 1995).
6. Stormer, H. L., Tsui, D. C. & Gossard, A. C. The fractional quantum hall effect. *Rev. Mod. Phys.* **71**, S298 (1999).
7. Stormer, H. L. Nobel lecture: the fractional quantum hall effect. *Rev. Mod. Phys.* **71**, 875 (1999).
8. Ardonne, E., Bergholtz, E. J., Kailasvuori, J. & Wikberg, E. Degeneracy of non-abelian quantum hall states on the torus: domain walls and conformal field theory. *J. Stat. Mech. Theory Exp.* **2008**, P04016 (2008).
9. Ardonne, E. & Regnault, N. Structure of spinful quantum hall states: a squeezing perspective. *Phys. Rev. B* **84**, 205134 (2011).
10. Lee, C. H., Ho, W. W., Yang, B., Gong, J. & Papić, Z. Floquet mechanism for non-abelian fractional quantum hall states. *Phys. Rev. Lett.* **121**, 237401 (2018).
11. Tournois, Y. & Ardonne, E. Braiding properties of paired spin-singlet and non-abelian hierarchy states. *J. Phys. A* **53**, 055402 (2020).
12. Tang, E., Mei, J.-W. & Wen, X.-G. High-temperature fractional quantum hall states. *Phys. Rev. Lett.* **106**, 236802 (2011).
13. Regnault, N. & Bernevig, B. A. Fractional chern insulator. *Phys. Rev.X* **1**, 021014 (2011).
14. Yao, N. Y. et al. Realizing fractional chern insulators in dipolar spin systems. *Phys. Rev. Lett.* **110**, 185302 (2013).
15. Lee, C. H. & Qi, X.-L. Lattice construction of pseudopotential hamiltonians for fractional chern insulators. *Phys. Rev. B* **90**, 085103 (2014).
16. Grushin, A. G., Gómez-León, Á. & Neupert, T. Floquet fractional chern insulators. *Phys. Rev. Lett.* **112**, 156801 (2014).
17. Yang, B., Hu, Z.-X., Lee, C. H. & Papić, Z. Generalized pseudopotentials for the anisotropic fractional quantum hall effect. *Phys. Rev. Lett.* **118**, 146403 (2017).
18. Abouelkomsan, A., Liu, Z. & Bergholtz, E. J. Particle-hole duality, emergent fermi liquids, and fractional chern insulators in moiré flatbands. *Phys. Rev. Lett.* **124**, 106803 (2020).
19. Yang, Z.-C., Liu, F., Gorshkov, A. V. & Iadecola, T. Hilbert-space fragmentation from strict confinement. *Phys. Rev. Lett.* **124**, 207602 (2020).
20. Sala, P., Rakovszky, T., Verresen, R., Knap, M. & Pollmann, F. Ergodicity breaking arising from hilbert space fragmentation in dipole-conserving hamiltonians. *Phys. Rev. X* **10**, 011047 (2020).
21. Patil, P. & Sandvik, A. W. Hilbert space fragmentation and ashkin-teller criticality in fluctuation coupled ising models. *Phys. Rev. B* **101**, 014453 (2020).
22. Langlett, C. M. & Xu, S. Hilbert space fragmentation and exact scars of generalized fredkin spin chains. *Phys. Rev. B* **103**, L220304 (2021).
23. Pietracaprina, F. & Laflorencie, N. Hilbert-space fragmentation, multifractality, and many-body localization. *Ann. Phys.* **435**, 168502 (2021).
24. Lee, K., Pal, A. & Changlani, H. J. Frustration-induced emergent hilbert space fragmentation. *Phys. Rev. B* **103**, 235133 (2021).
25. Lee, T. E. Anomalous edge state in a non-hermitian lattice. *Phys. Rev. Lett.* **116**, 133903 (2016).
26. Gong, Z. et al. Topological phases of non-hermitian systems. *Phys. Rev. X* **8**, 031079 (2018).
27. Yao, S. & Wang, Z. Edge states and topological invariants of non-hermitian systems. *Phys. Rev. Lett.* **121**, 086803 (2018).
28. Lee, C. H. & Thomale, R. Anatomy of skin modes and topology in non-hermitian systems. *Phys. Rev. B* **99**, 201103 (2019).
29. Yokomizo, K. & Murakami, S. Non-bloch band theory of non-hermitian systems. *Phys. Rev. Lett.* **123**, 066404 (2019).
30. Lee, C. H., Li, L., Thomale, R. & Gong, J. Unraveling non-hermitian pumping: emergent spectral singularities and anomalous responses. *Phys. Rev. B* **102**, 085151 (2020).
31. Helbig, T. et al. Generalized bulk–boundary correspondence in non-hermitian topolectrical circuits. *Nat. Phys.* **16**, 747–750 (2020).
32. Schomerus, H. Nonreciprocal response theory of non-hermitian mechanical metamaterials: Response phase transition from the skin effect of zero modes. *Phys. Rev. Res.* **2**, 013058 (2020).
33. Li, L. & Lee, C. H. Non-Hermitian pseudo-gaps. *Science Bulletin* **67**, 685–690 (2022).
34. Song, F., Yao, S. & Wang, Z. Non-hermitian skin effect and chiral damping in open quantum systems. *Phys. Rev. Lett.* **123**, 170401 (2019).
35. Borgnia, D. S., Kruchkov, A. J. & Slager, R.-J. Non-hermitian boundary modes and topology. *Phys. Rev. Lett.* **124**, 056802 (2020).
36. Zhang, K., Yang, Z. & Fang, C. Correspondence between winding numbers and skin modes in non-hermitian systems. *Phys. Rev. Lett.* **125**, 126402 (2020).
37. Okuma, N., Kawabata, K., Shiozaki, K. & Sato, M. Topological origin of non-hermitian skin effects. *Phys. Rev. Lett.* **124**, 086801 (2020).
38. Kawabata, K., Sato, M. & Shiozaki, K. Higher-order non-hermitian skin effect. *Phys. Rev. B* **102**, 205118 (2020).
39. Ghatak, A., Brandenbourger, M., van Wezel, J. & Coulais, C. Observation of non-hermitian topology and its bulk–edge correspondence in an active mechanical metamaterial. *Proc. Natl Acad. Sci. USA* **117**, 29561–29568 (2020).
40. Xiao, L. et al. Non-hermitian bulk–boundary correspondence in quantum dynamics. *Nat. Phys.* **16**, 761–766 (2020).
41. Longhi, S. Non-bloch-band collapse and chiral zener tunneling. *Phys. Rev. Lett.* **124**, 066602 (2020).
42. Mu, S., Lee, C. H., Li, L. & Gong, J. Emergent fermi surface in a many-body non-hermitian fermionic chain. *Phys. Rev. B* **102**, 081115 (2020).
43. Lee, C. H. & Longhi, S. Ultrafast and anharmonic Rabi oscillations between non-Bloch bands. *Communications Physics* **3**, 1–9 (2020).
44. Zou, D. et al. Observation of hybrid higher-order skin-topological effect in non-Hermitian topolectrical circuits. *Nat. Commun.* **12**, 1–11 (2021).
45. Okuma, N. & Sato, M. Quantum anomaly, non-hermitian skin effects, and entanglement entropy in open systems. *Phys. Rev. B* **103**, 085428 (2021).
46. Berry, M. V. Physics of nonhermitian degeneracies. *Czechoslov. J. Phys.* **54**, 1039–1047 (2004).
47. Heiss, W. The physics of exceptional points. *J. Phys. A* **45**, 444016 (2012).
48. Wu, J.-H., Artoni, M. & La Rocca, G. Non-hermitian degeneracies and unidirectional reflectionless atomic lattices. *Phys. Rev. Lett.* **113**, 123004 (2014).
49. Heiss, D. Circling exceptional points. *Nat. Phys.* **12**, 823–824 (2016).
50. Kozii, V. & Fu, L. Non-Hermitian topological theory of finite-lifetime quasiparticles: prediction of bulk Fermi arc due to exceptional point. arXiv preprint arXiv:1708.05841 (2017).
51. Leykam, D., Bliokh, K. Y., Huang, C., Chong, Y. D. & Nori, F. Edge modes, degeneracies, and topological numbers in non-hermitian systems. *Phys. Rev. Lett.* **118**, 040401 (2017).
52. Hodaei, H. et al. Enhanced sensitivity at higher-order exceptional points. *Nature* **548**, 187–191 (2017).
53. Wang, S. et al. Arbitrary order exceptional point induced by photonic spin–orbit interaction in coupled resonators. *Nat. Commun.* **10**, 1–9 (2019).
54. Lafalce, E. et al. Robust lasing modes in coupled colloidal quantum dot microdisk pairs using a non-hermitian exceptional point. *Nat. Commun.* **10**, 1–8 (2019).
55. Okugawa, R. & Yokoyama, T. Topological exceptional surfaces in non-hermitian systems with parity-time and parity-particle-hole symmetries. *Phys. Rev. B* **99**, 041202 (2019).
56. Yoshida, T., Peters, R., Kawakami, N. & Hatsugai, Y. Symmetry-protected exceptional rings in two-dimensional correlated systems with chiral symmetry. *Phys. Rev. B* **99**, 121101 (2019).

57. Yoshida, T. & Hatsugai, Y. Exceptional rings protected by emergent symmetry for mechanical systems. *Phys. Rev. B* **100**, 054109 (2019).
58. Lee, C. H. Exceptional bound states and negative entanglement entropy. *Phys. Rev. Lett.* **128**, 010402 (2022).
59. Park, S. H. et al. Observation of an exceptional point in a non-hermitian metasurface. *Nanophotonics* **9**, 1031–1039 (2020).
60. Yoshida, T., Peters, R. & Kawakami, N. Non-hermitian perspective of the band structure in heavy-fermion systems. *Phys. Rev. B* **98**, 035141 (2018).
61. Yao, S., Song, F. & Wang, Z. Non-hermitian chern bands. *Phys. Rev. Lett.* **121**, 136802 (2018).
62. Lourenço, J. A., Eneias, R. L. & Pereira, R. G. Kondo effect in a pt-symmetric non-hermitian hamiltonian. *Phys. Rev. B* **98**, 085126 (2018).
63. Kawabata, K., Okuma, N. & Sato, M. Non-bloch band theory of non-hermitian hamiltonians in the symplectic class. *Phys. Rev. B* **101**, 195147 (2020).
64. Yokomizo, K. & Murakami, S. Non-bloch band theory and bulk–edge correspondence in non-hermitian systems. *Prog. Theor. Exp. Phys.* **2020**, 12A102 (2020).
65. Nagai, Y., Qi, Y., Isobe, H., Kozii, V. & Fu, L. Dmft reveals the non-hermitian topology and fermi arcs in heavy-fermion systems. *Phys. Rev. Lett.* **125**, 227204 (2020).
66. Zhu, X. et al. Photonic non-hermitian skin effect and non-bloch bulk-boundary correspondence. *Phys. Rev. Res.* **2**, 013280 (2020).
67. Nakagawa, M., Kawakami, N. & Ueda, M. Non-hermitian kondo effect in ultracold alkaline-earth atoms. *Phys. Rev. Lett.* **121**, 203001 (2018).
68. Hamazaki, R., Kawabata, K. & Ueda, M. Non-hermitian many-body localization. *Phys. Rev. Lett.* **123**, 090603 (2019).
69. Liu, T., He, J. J., Yoshida, T., Xiang, Z.-L. & Nori, F. Non-hermitian topological mott insulators in one-dimensional fermionic superlattices. *Phys. Rev. B* **102**, 235151 (2020).
70. Zhang, D.-W. et al. Skin superfluid, topological mott insulators, and asymmetric dynamics in an interacting non-hermitian aubry-andré-harper model. *Phys. Rev. B* **101**, 235150 (2020).
71. Xi, W., Zhang, Z.-H., Gu, Z.-C. & Chen, W.-Q. Classification of topological phases in one dimensional interacting non-hermitian systems and emergent unitarity. *Sci. Bull.* **66**, 1731–1739 (2021).
72. Zhai, L.-J., Yin, S. & Huang, G.-Y. Many-body localization in a non-hermitian quasiperiodic system. *Phys. Rev. B* **102**, 064206 (2020).
73. Yoshida, T. & Hatsugai, Y. Correlation effects on non-hermitian point-gap topology in zero dimension: Reduction of topological classification. *Phys. Rev. B* **104**, 075106 (2021).
74. Lee, C. H. Many-body topological and skin states without open boundaries. *Phys. Rev. B* **104**, 195102 (2021).
75. Li, L., Lee, C. H., Mu, S. & Gong, J. Critical non-hermitian skin effect. *Nat. Commun.* **11**, 1–8 (2020).
76. Stone, M. *Quantum Hall Effect* (World Scientific, 1992).
77. Kapit, E. & Mueller, E. Exact parent hamiltonian for the quantum hall states in a lattice. *Phys. Rev. Lett.* **105**, 215303 (2010).
78. Chung, H., Huang, Y., Lee, M., Chang, C. & Lin, M. Quasi-landau levels in bilayer zigzag graphene nanoribbons. *Physica E: Low Dimens. Syst. Nanostruct.* **42**, 711–714 (2010).
79. Rhim, J.-W. & Kim, Y. B. Landau level quantization and almost flat modes in three-dimensional semimetals with nodal ring spectra. *Phys. Rev. B* **92**, 045126 (2015).
80. Wang, C., Sun, H.-P., Lu, H.-Z. & Xie, X. 3d quantum hall effect of fermi arcs in topological semimetals. *Phys. Rev. Lett.* **119**, 136806 (2017).
81. Rhim, J.-W., Kim, K. & Yang, B.-J. Quantum distance and anomalous landau levels of flat bands. *Nature* **584**, 59–63 (2020).
82. Hudomal, A., Vasić, I., Regnault, N. & Papić, Z. Quantum scars of bosons with correlated hopping. *Commun. Phys.* **3**, 1–12 (2020).
83. Lieu, S. Topological phases in the non-hermitian su-schrieffer-heeger model. *Phys. Rev. B* **97**, 045106 (2018).
84. Marques, A. & Dias, R. Topological bound states in interacting su–schrieffer–heeger rings. *J. Phys. Condens. Matter* **30**, 305601 (2018).
85. Pietracaprina, F. & Laflorencie, N. Hilbert-space fragmentation, multifractality, and many-body localization. *Annals of Physics* **435**, 168502 (2021).
86. Lee, K., Pal, A. & Changlani, H. J. Frustration-induced emergent hilbert space fragmentation. *Phys. Rev. B* **103**, 235133 (2021).
87. Herviou, L., Bardarson, J. H. & Regnault, N. Many-body localization in a fragmented hilbert space. *Phys. Rev. B* **103**, 134207 (2021).
88. Pan, L., Chen, X., Chen, Y. & Zhai, H. Non-hermitian linear response theory. *Nat. Phys.* **16**, 767–771 (2020).
89. Rakovszky, T., Sala, P., Verresen, R., Knap, M. & Pollmann, F. Statistical localization: from strong fragmentation to strong edge modes. *Phys. Rev. B* **101**, 125126 (2020).
90. Choi, S. et al. Emergent su (2) dynamics and perfect quantum many-body scars. *Phys. Rev. Lett.* **122**, 220603 (2019).
91. Zhao, H., Vovrosh, J., Mintert, F. & Knolle, J. Quantum many-body scars in optical lattices. *Phys. Rev. Lett.* **124**, 160604 (2020).
92. Turner, C. J., Michailidis, A. A., Abanin, D. A., Serbyn, M. & Papić, Z. Weak ergodicity breaking from quantum many-body scars. *Nat. Phys.* **14**, 745–749 (2018).
93. Turner, C., Michailidis, A., Abanin, D., Serbyn, M. & Papić, Z. Quantum scarred eigenstates in a rydberg atom chain: Entanglement, breakdown of thermalization, and stability to perturbations. *Phys. Rev. B* **98**, 155134 (2018).
94. Turner, C. J., Desaules, J. Y., Bull, K. & Papić, Z. Correspondence principle for many-body scars in ultracold Rydberg atoms. *Phys. Rev. X* **11**, 021021 (2021).
95. Pal, A. & Huse, D. A. Many-body localization phase transition. *Phys. Rev. B* **82**, 174411 (2010).
96. Nandkishore, R. & Huse, D. A. Many-body localization and thermalization in quantum statistical mechanics. *Annu. Rev. Condens. Matter Phys.* **6**, 15–38 (2015).
97. Alet, F. & Laflorencie, N. Many-body localization: an introduction and selected topics. *Comptes Rendus Phys.* **19**, 498–525 (2018).
98. Zhao, H., Knolle, J. & Mintert, F. Engineered nearest-neighbor interactions with doubly modulated optical lattices. *Phys. Rev. A* **100**, 053610 (2019).
99. McArdle, S. et al. Variational ansatz-based quantum simulation of imaginary time evolution. *npj Quant. Inform.* **5**, 1–6 (2019).
100. Lin, S.-H., Dilip, R., Green, A. G., Smith, A. & Pollmann, F. Real-and imaginary-time evolution with compressed quantum circuits. *PRX Quant.* **2**, 010342 (2021).
101. Lee, C. H. et al. Topolectrical circuits. *Commun. Phys.* **1**, 1–9 (2018).
102. Olekhno, N. A. et al. Topological edge states of interacting photon pairs emulated in a topolectrical circuit. *Nat. Commun.* **11**, 1–8 (2020).
103. Lee, C. H. et al. Imaging nodal knots in momentum space through topolectrical circuits. *Nat. Commun.* **11**, 1–13 (2020).
104. Liu, S. et al. Octupole corner state in a three-dimensional topological circuit. *Light Sci. Appl.* **9**, 1–9 (2020).
105. Yang, Y., Zhu, D., Hang, Z. & Chong, Y. Observation of antichiral edge states in a circuit lattice. *Science China Physics, Mechanics & Astronomy* **64**, 1–7 (2021).
106. Wang, Y., Price, H. M., Zhang, B. & Chong, Y. Circuit implementation of a four-dimensional topological insulator. *Nat. Commun.* **11**, 1–7 (2020).
107. Stegmaier, A. et al. Topological defect engineering and p t symmetry in non-hermitian electrical circuits. *Phys. Rev. Lett.* **126**, 215302 (2021).
108. Weinberg, P. & Bukov, M. QuSpin: a Python package for dynamics and exact diagonalisation of quantum many body systems part I: spin chains. *SciPost Physics* **2**, 003 (2017).
109. Weinberg, P. & Bukov, M. Quspin: a python package for dynamics and exact diagonalisation of quantum many body systems. part ii: bosons, fermions and higher spins. *SciPost Phys* **7**, 97 (2019).

Acknowledgements

We thank Hui Jiang and Yin Zhong for discussions. The Hamiltonians are numerically computed with QuSpin[108,109], and R.S. thank Phillip Weinberg for providing suggestions on the computational programming. This work is supported by the MOE Tier I start-up grant WBS: R-144-000-435-133.

Author contributions

C.H.L. carried out preliminary studies and supervised the project. R.S. carried out additional theoretical and computational studies. Both authors discussed the results and participated in the writing of the manuscript.

Competing interests

The authors declare no competing interests.

Additional information

Supplementary information The online version contains supplementary material available at https://doi.org/10.1038/s42005-022-01015-w.

Correspondence and requests for materials should be addressed to Ching Hua Lee.

Peer review information *Communications Physics* thanks the anonymous reviewers for their contribution to the peer review of this work.